Nano Research

Open Access

Research Article

Facet-selective etching by pyridazine toward robust ruthenium-based oxygen evolution catalysts

Xueting Cao[§], Yikun Kang[§], Tao Jiang, Zhe Chen, Yaming Hao, Shuangshuang Cha, Wei Du, Yefei Li ✉, and Ming Gong ✉

Department of Chemistry, Shanghai Key Laboratory of Molecular Catalysis and Innovative Materials and Collaborative Innovation Center of Chemistry for Energy Materials (iChEM), Fudan University, Shanghai 200438, China
[§] Xueting Cao and Yikun Kang contributed equally to this work.

Cite this article: *Nano Research*, **2025**, *18*, 94907315. https://doi.org/10.26599/NR.2025.94907315

ABSTRACT: Stable oxygen evolution reaction (OER) catalyst alternatives to the precious IrO_2 catalysts are of great importance to the next-generation proton-exchange membrane (PEM) electrolyzers. RuO_2-based materials are promising candidates but suffer from low stability under highly anodic potentials. Here, we reported a facet-selective etching strategy to improve the stability of polycrystalline RuO_2 without significantly affecting the activity. The selective etching was enabled by the specific chemisorption of pyridazine (pyd) with contingent N atoms onto the RuO_2 surface. The pyd-RuO_2 catalyst, after etching, exhibited a low overpotential 247 mV at 100 mA·cm^{-2} and obvious stability improvement of over 200 h at 100 mA·cm^{-2} with only 0.63% Ru loss in acidic conditions. Combining various characterization techniques and theoretical calculations, we revealed that the crystalline RuO_2 (110) facet is favorably etched by the coordination of pyridazine while protecting other surfaces, which significantly enriches the RuO_2 (110) facets toward higher OER stability via the dynamic dissolution and repair mechanism in the ordered manner. This study offers alternative perspectives on the dissolution and stability mechanism of RuO_2 and the facet-selective modulation of nanocrystals by ligand-driven etching.

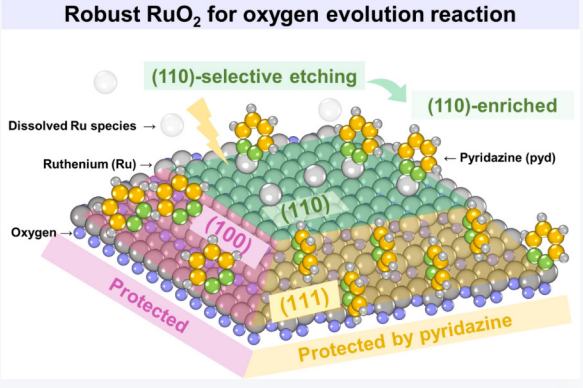

KEYWORDS: ruthenium dioxide, oxygen evolution reaction, stability, pyridazine, facet-selective etching

1 Introduction

Oxygen evolution reaction (OER), as the anodic half reaction of water electrolysis, is one of the crucial limiting steps for green hydrogen production [1, 2]. The sluggish process of 4e$^-$ transfer to produce one dioxygen molecule significantly constrains the overall efficiency of water electrolysis [3, 4]. To improve this efficiency, one of the most recognized approaches is to develop highly-active OER catalysts to reduce the anodic overpotential. Considering the actual application scenario, OER in proton exchange membrane (PEM) electrolyzers is characterized by strong oxidative and acidic environment [5]. This often limits the choice of OER catalysts to precious noble-metal-based catalysts. Compared to the widely-adopted iridium (Ir)-based catalysts, ruthenium (Ru)-based catalysts (e.g., ruthenium dioxide (RuO_2)) are considerably more cost-effective and exhibit higher OER activities, but their greater tendency toward dissolution or surface reconstruction under anodic condition limits its potential application [6, 7].

From a macroscopic and thermodynamic perspective, RuO_2 can be oxidized to soluble $[RuO_4]^{2-}$ and even high-valent $[RuO_4]$ under anodic potentials (above 1.5 V vs. reversible hydrogen electrode (RHE)) [8, 9]. Researchers have been dedicated to constraining the Ru–O moieties within the catalysts to overcome the deactivation problem. Some effective strategies include (1) doping RuO_2 with oxyphilic elements (Mn, W, Co, Ni, Zn, Si, B, Sn, Cr, Nb, etc.) [10–20], (2) introducing metal–substrate interactions [21–23], (3) constructing special RuO_2 structures [24–27], or (4) modifying the surface [28, 29]. These strategies can tailor the electron densities and redox states of Ru and O, thus altering the thermodynamic characteristics of Ru-based catalysts toward higher stability.

Received: January 23, 2025; **Revised:** February 19, 2025
Accepted: February 20, 2025

✉Address correspondence to Yefei Li, yefeil@fudan.edu.cn; Ming Gong, gongm@fudan.edu.cn

From the microscopic and dynamic perspective, less advance has been made to understand the molecular mechanism of Ru dissolution and its instability toward OER, and the proposed mechanisms are still in debate and have not yet turned into mechanism-driven optimization strategies. For instance, Alexandrov et al. [30] believed that both Ru dissolution and OER processes experience the same $RuO_2(OH)$ and $RuO_2(OH)_2$ intermediates, making instability inevitable. In contrast, the experiments conducted by Stephens et al. [31] demonstrated that the number of defects decreases over time until reaching a more stable state. Consequently, they were able to differentiate the OER active sites and the corrosion-prone sites. Despite the yet reached consensus, one of the common views is that the stability of RuO_2 is relevant to crystal surface orientation that tailors the Ru–O bond strength. Specifically, RuO_2 (110) is often favorably produced due to its lower free energy and exhibits higher stability than other facets [32]. However, these studies are often based on theoretical calculation or model single-crystal RuO_2 surfaces, which possess large discrepancy with the widely-used polycrystalline catalysts. Accordingly, enriching the facets and gleaning the molecular-level mechanism of the facet-specific activity and stability remains a challenging task but can inspire more rational optimization strategies toward cost-effective and robust OER catalysts.

The different atomic arrangements on different facets can specifically interact with certain adsorbate molecules to enable the facet-selective growth of nanocrystals. For example, polyvinylpyrrolidone preferentially passivates high-surface-energy Ag {100} facets via van der Waals interactions while stabilizing Ag {111} through stronger covalent coordination [33]. However, existing studies predominantly focus on either (i) additive-mediated crystallographic control during material synthesis or (ii) surface restructuring of RuO_2 induced by adsorbed oxygen species during OER [34–36]. In contrast, the electrochemical etching of RuO_2 surfaces by non-oxygen adsorbates, a critical mechanism for modulating surface structure to enhance OER stability, remains relatively underexplored. Inspired by this, we envision that the introduction of specific adsorbates into the electrolytic systems can induce the facet-selective etching of polycrystalline RuO_2 catalysts. This could enable the facet-enriching RuO_2 catalyst electrode and provide an essential platform for gleaning the molecular-level mechanism. Correspondingly, we have identified a coordinative additive of pyridazine (pyd, $C_4H_4N_2$), a heterocyclic molecule with two neighboring nitrogen atoms, as a monodentate or a bidentate ligand for the facet-selective etching of RuO_2 at low concentrations (< 1 mmol·L^{-1}) in acidic media [37]. This etching process selectively etched the RuO_2 (110) surface while protecting other crystalline facets under the harsh electrochemical treatments, thus enriching the RuO_2 (110) and enhancing the overall long-term stability. Based on this catalyst platform, an exhaustive analysis of the mechanism that underpins the facet-selective durability of RuO_2 as well as the facet-selective etching process was conducted and supported by transmission electron microscopy (TEM), X-ray photoelectron spectroscopy (XPS), *in situ* attenuated total reflection surface-enhanced infrared absorption spectroscopy (ATR-SEIRAS), kinetics analysis, and density functional theory (DFT) calculations. This study not only opens up a new method of enriching specific facets on oxide catalysts but also offers a unique platform for the in-depth investigation of Ru-centered OER activity and stability mechanism.

2 Results and discussion

Polycrystalline RuO_2 catalyst precursors were prepared by a typical hydrothermal method [38]. These precursors were then drop-casted onto the carbon fiber papers (CFPs) and annealed at 300 °C for 1 h to give the RuO_2/CFP electrodes. An electrochemical etching step in the pyridazine-containing electrolyte was further adopted to selectively etch the RuO_2 catalyst under anodic potentials to produce the pyd-RuO_2/CFP electrode (Fig. 1(a)). The optimal experimental parameters, including pyridazine concentration, electrode potential, and etching time, were screened and determined with relevant details provided in methods and Figs. S1–S3 in the Electronic Supplementary Material (ESM). The optimal condition involves the addition of 20 μL pyridazine in 50 mL 0.5 mol·L^{-1} H_2SO_4 (5.5 mmol·L^{-1} pyridazine) and an applied potential of 1.6 V vs. Ag/AgCl for 300 s.

We first characterized the RuO_2 and pyd-RuO_2 catalysts to confirm the selective etching process. Both catalysts exhibit polycrystalline structures rich in grain boundaries with nanoscale crystal domains (Figs. 1(b) and 1(c)) and maintain the rutile structure according to the selected area electron diffraction (SAED) pattern (Fig. S4 in the ESM) [39, 40]. To evaluate the etching effect on the lattices, we counted the four different crystalline lattice stripes (e.g. (101), (110), (111), and (200)) in the TEM images of RuO_2 before and after pyridazine-driven etching. After etching, the (110) lattice stripes of pyd-RuO_2 were significantly reduced, with the increasing percentages of (101) and (200) lattice stripes (Fig. 1(d)). Considering the correlation between three-dimensional spatial structures and lattice stripes (Fig. S5 in the ESM), the lower probabilities of (110) lattice stripes actually indicate the enrichment of the (110) facet toward a more stable RuO_2 (110) structure. The absence of pyridazine led to a less-pronounced enrichment effect, and the remnant N from the pyridazine on pyd-RuO_2 was revealed by the energy-dispersive spectroscopy (EDS) (Fig. S6 in the ESM), which supports the interaction between pyridazine and the RuO_2 surface likely by chemisorption. This probable facet-selective chemisorption then induces the face-selective etching of RuO_2 catalysts toward a RuO_2 (110)-centered surface structure.

Further surface chemical identities of the RuO_2 and pyd-RuO_2 catalysts were analyzed by XPS (Figs. 1(e) and 1(f)). The Ru $3p_{3/2}$ spectra could be deconvoluted into two major peaks, corresponding to Ru^{4+} and Ru^{3+} or Ru^{5+} species [11, 41, 42]. The peak at higher binding energy is typically attributed to Ru^{3+} due to the instability of Ru^{5+} species, but our selective etching method involves the treatment at highly anodic potentials, which possibly generates Ru^{5+} on the surface. By integrating the deconvoluted peaks, we derived the relative ratio of each species (Figs. 1(g) and 1(h)). The pyridazine etching treatment increased the proportion of the more stable Ru^{4+} species from 65.8% to 73.1%, likely due to the highly anodic potentials applied for etching unstable Ru^{3+}/Ru^{5+}. As the pyd-RuO_2 was utilized for OER, this proportion of Ru^{4+} slightly diminished from 73.1% to 65.3% while from 65.8% to 51.6% for RuO_2. As for the O 1s spectra, the peaks could be deconvoluted and ascribed to lattice oxygen O^{2-}, the hydroxyl species (OH) and the water or oxygen vacancies (H_2O/O_{vac}) from lower binding energies to higher binding energies (Fig. 1(f)) [43, 44]. The pyridazine treatment resulted in the significant loss of O^{2-} and the increasing fraction of OH, which corresponds to pyridazine-driven leaching of Ru and lattice O^{2-}. Further OER treatment diminished the OH

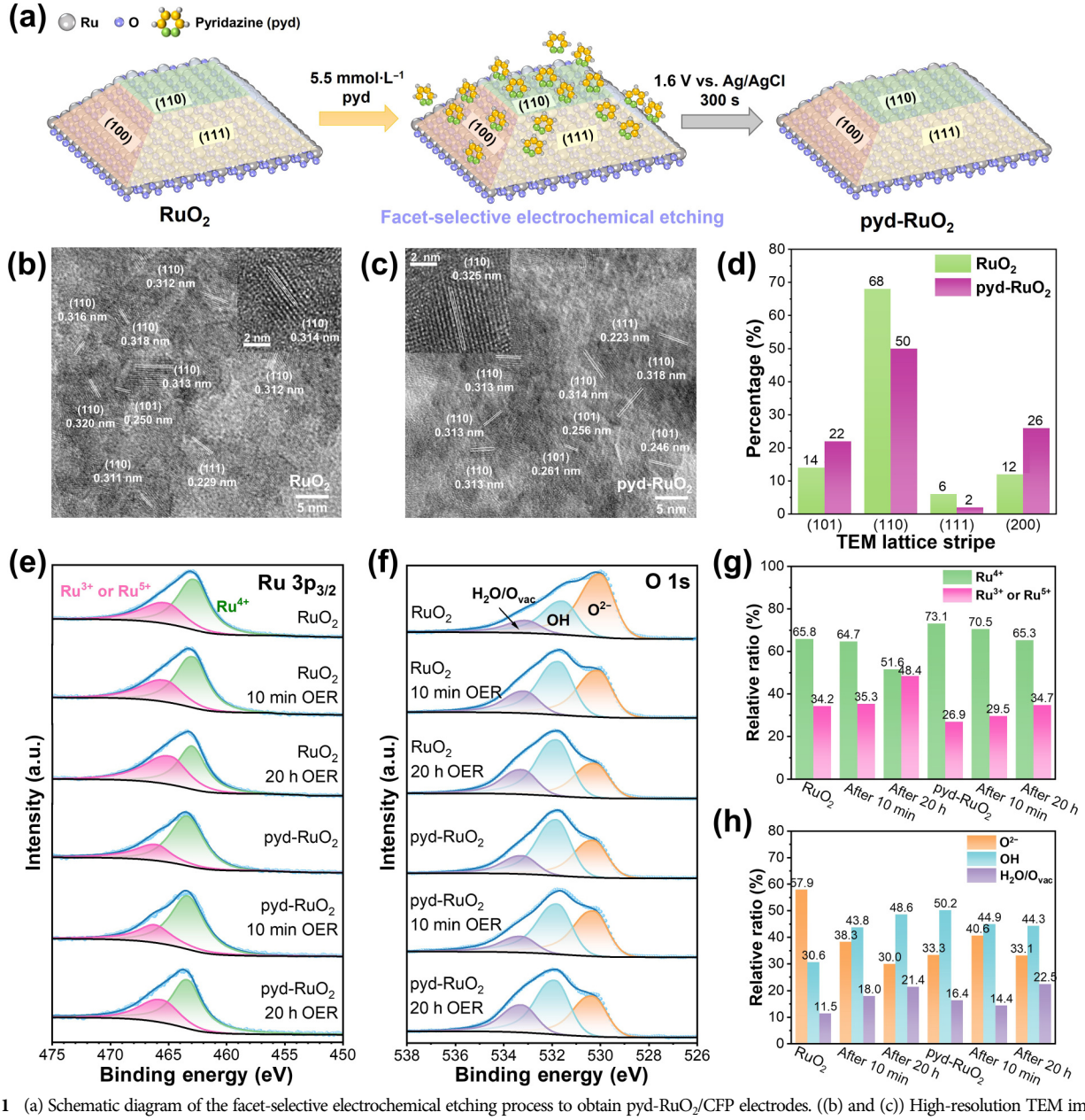

Figure 1 (a) Schematic diagram of the facet-selective electrochemical etching process to obtain pyd-RuO_2/CFP electrodes. ((b) and (c)) High-resolution TEM images of (b) RuO_2 and (c) pyd-RuO_2. (d) The comparation of related crystal indexes ratios from TEM images. (e) Ru $3p_{3/2}$ and (f) O 1s XPS spectra of RuO_2/CFP, RuO_2/CFP-10 min, RuO_2/CFP-20 h, pyd-RuO_2/CFP, pyd-RuO_2/CFP-10 min, and pyd-RuO_2/CFP-20 h. ((g) and (h)) The relative deconvoluted area ratios of Ru^{4+} and Ru^{3+}/Ru^{5+}, and those of O^{2-}, OH, and H_2O for each catalyst in (e) and (f).

species and generated more O^{2-} and H_2O/O_{vac}, presumably resulting from the surface reconstruction during OER. Furthermore, a semi-quantitative XPS analysis revealed the increasing N peak intensity after pyridazine treatment due to its chemisorption (Fig. S7 in the ESM), but as the OER reaction progressed, this N 1s peak underwent a gradual decrease, approaching a state akin to RuO_2/CFP, which suggests the detachment of pyridazine during OER in a pyridazine-free electrolyte.

We then evaluated the stability and activity of the pristine RuO_2/CFP electrode and pyd-RuO_2/CFP electrode (Figs. 2(a) and 2(b)). An etched RuO_2/CFP in the H_2SO_4 electrolyte without pyridazine (H_2SO_4-RuO_2/CFP) was also compared side-by-side. At a loading of 0.4 mg·cm^{-2}, the pyd-RuO_2/CFP electrode showed obvious stability improvement at a current density of 100 mA·cm^{-2} (Fig. 2(a)). The stability curve manifests a distinctive plateau region for the first 15 h with a slow decay afterwards. In stark contrast, the RuO_2/CFP and H_2SO_4-RuO_2/CFP electrodes showed obvious decay within 30 h, with potential ramping up to > 1.7 V vs. RHE. As for activity, both RuO_2/CFP and pyd-RuO_2/CFP electrodes presented high OER activities with very slight activity differences. Specifically, the pyd-RuO_2/CFP possessed the low overpotentials of 187 mV at 10 mA·cm^{-2} and 247 mV at 100 mA·cm^{-2} (Fig. 2(b)). The Tafel analysis revealed that the very slight increase in the Tafel slope from 43.57 to 46.62 mV·dec^{-1} after pyridazine etching did not have a significant blunting effect on the OER reaction kinetics (Fig. S8 in the ESM). In Bode plots, the peaks of phase angles appeared at the identical frequencies for RuO_2/CFP and pyd-RuO_2/CFP, suggesting the negligible effect of etching on the reaction mechanisms, but the

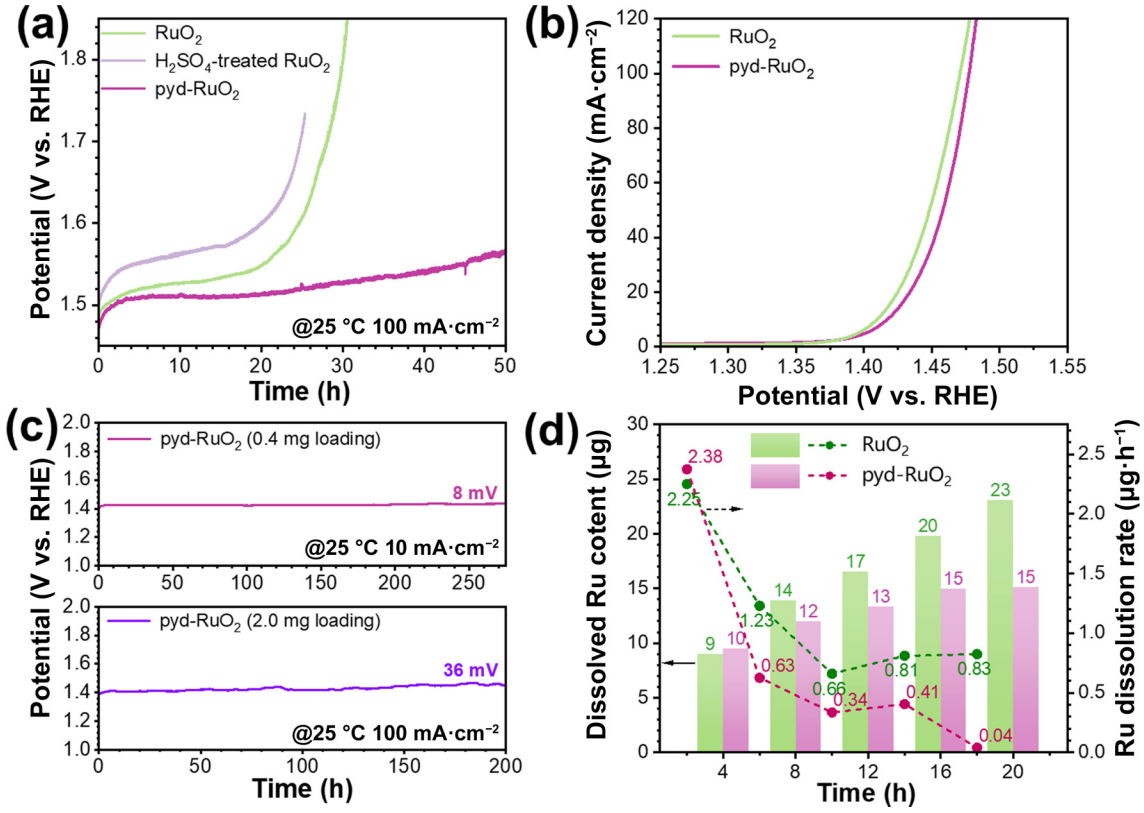

Figure 2 (a) The chronopotentiometric curves of RuO_2/CFP, H_2SO_4-RuO_2/CFP, and pyd-RuO_2/CFP at a loading of 0.4 mg·cm^{-2} RuO_2. (b) Linear sweep voltammetry curves of RuO_2/CFP and pyd-RuO_2/CFP, at a loading of 0.4 mg·cm^{-2} RuO_2 and under a scan rate of 5 mV·s^{-1}. (c) The chronopotentiometric curves with pyd-RuO_2/CFP at a loading of 0.4 mg·cm^{-2} RuO_2 and a constant current density of 10 mA·cm^{-2} and with pyd-RuO_2/CFP at a loading of 2 mg·cm^{-2} at 100 mA·cm^{-2}. (d) Ru dissolution contents and dissolution rates for RuO_2/CFP and pyd-RuO_2/CFP under 100 mA·cm^{-2} electrolysis conditions.

charge-transfer resistance was slightly lowered for pyd-RuO_2/CFP, as indicated by the Nyquist plots (Fig. S9 in the ESM).

To further illustrate the stability enhancement by pyridine etching, we conducted long-term stability tests on pyd-RuO_2/CFP. The pyd-RuO_2/CFP showed over 250 h stability with a decay of only 8 mV at 10 mA·cm^{-2} under the loading of 0.4 mg·cm^{-2} and over 200 h stability with a decay of 36 mV at 100 mA·cm^{-2} under the loading of 2.0 mg·cm^{-2} (Fig. 2(c)). In the latter case, only 0.63% Ru dissolved in the H_2SO_4 electrolyte. We further compared the dissolution of Ru for RuO_2/CFP and pyd-RuO_2/CFP during electrolysis under 100 mA·cm^{-2} by quantifying the dissolved Ru in the electrolyte at 4 h intervals (Fig. S10 and Table S1 in the ESM). After 20 h of OER, the content of dissolved Ru for pyd-RuO_2/CFP was significantly lower than that for RuO_2/CFP, and the dissolution rate for pyd-RuO_2/CFP decreased dramatically from 2.38 to 0.04 μg·h^{-1} (Fig. 2(d)). Both catalyst electrodes showed dramatic Ru dissolution during the initial 4 h and stabilized after the 4 h period. During the stabilized period, the pyd-RuO_2/CFP showed significantly lower Ru dissolution rates than RuO_2/CFP to contribute to the higher stability. This likely originated from the enriched RuO_2 (110) facets upon pyridazine etching, and the proposed mechanism will be elaborated later. These results indicate the efficacy of the pyridazine-induced facet-selective electrochemical etching method in enhancing the stability of RuO_2 catalysts.

To further demonstrate the pyridazine effect during etching and its stability enhancement effect, we carried more detailed analysis by electrochemical methods and *in situ* spectroscopy. If pyridazine remains in the electrolyte during OER, the activity is greatly suppressed with increasing potentials to drive the constant current density (Fig. 3(a)). It indicates that pyridazine has a very strong adsorption capability on the RuO_2 surface toward poisoning the OER-active sites, which, in the meantime, suggests that the etching process is dominated by the chemisorption of pyridazine on the surface. We further conducted the cyclic voltammetry (CV) analysis on RuO_2/CFP and pyd-RuO_2/CFP electrodes in a wider potential window and compared the fifth CV cycles of the two electrodes (Figs. 3(b) and 3(c)). Two pairs of redox peaks were observed: the Ru^{3+}/Ru^{4+} redox at 0.6 V vs. RHE and the Ru^{4+}/Ru^{5+} redox at 1.2 V vs. RHE [11, 45]. The Ru^{3+}/Ru^{4+} and Ru^{4+}/Ru^{5+} peaks of pyd-RuO_2/CFP slightly shifted toward more positive potentials compared to those of RuO_2/CFP. This shift represents the higher binding of surface Ru to the catalyst with more reluctance for oxidation and dissolution. Meanwhile, the peak areas for both sets of Ru redox decreased upon pyridazine treatment, suggesting an enhancement in the Ru stability. Moreover, the repetitive CV scans showed a gradual increase of capacitance for the pristine RuO_2 in the H_2SO_4 electrolyte but a relatively steady capacitance for the pyd-RuO_2/CFP. While performing the identical repetitive scans on RuO_2/CFP but in the electrolyte of 5.5 mmol·L^{-1} pyridazine + 0.5 mol·L^{-1} H_2SO_4, we also observed the greatly-maintained capacitance (Fig. S11 in the ESM), supporting the stabilizing effect of pyridazine.

We also employed the *in situ* ATR-SEIRAS technique to characterize the interface during etching and OER. First, the Au electrode with RuO_2 coating was submerged in a 0.5 mol·L^{-1} H_2SO_4 electrolyte containing 5.5 mmol·L^{-1} pyridazine and spectra were collected at potentials ranging from 0.95 to 1.25 V vs. AgCl

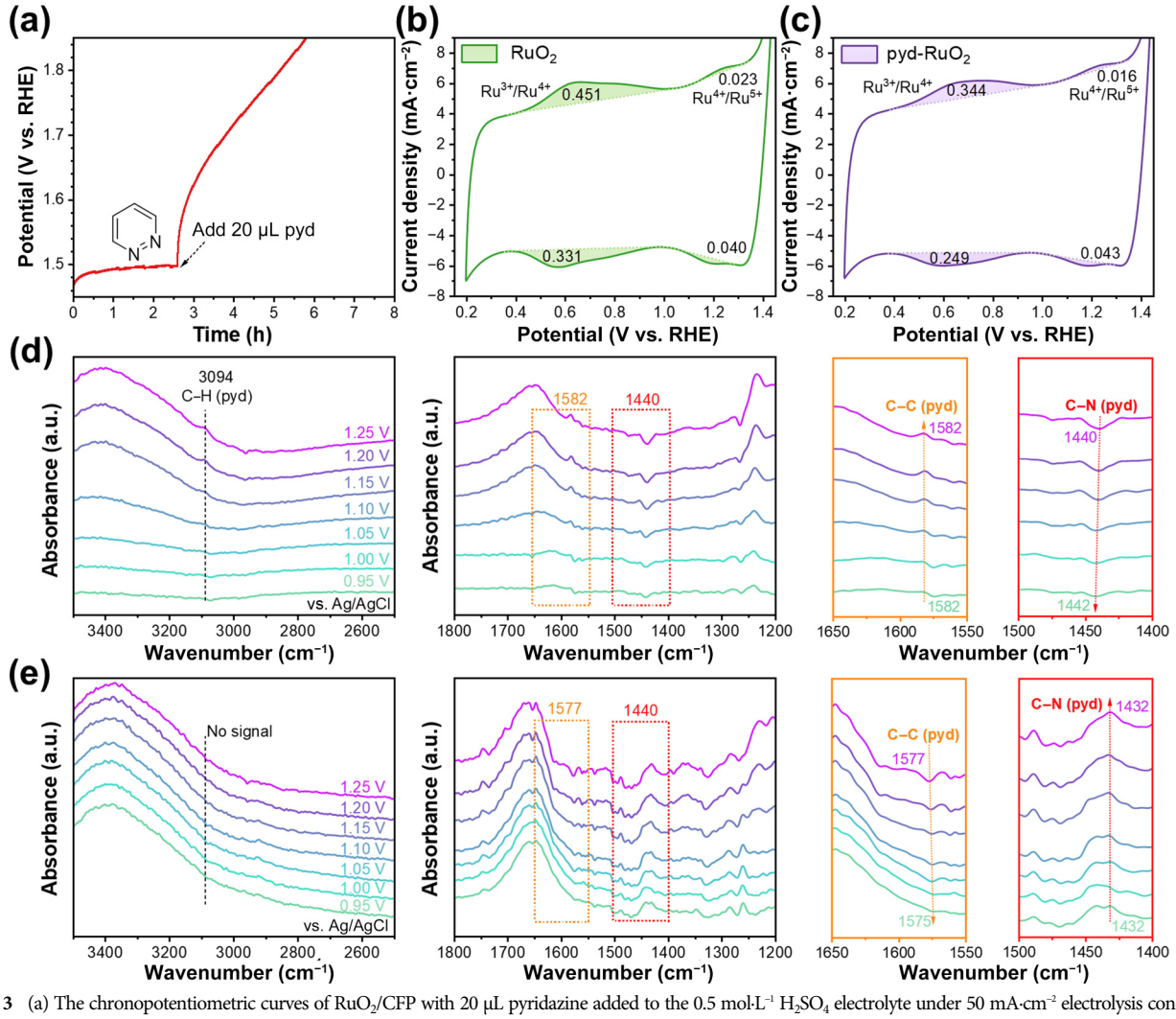

Figure 3 (a) The chronopotentiometric curves of RuO_2/CFP with 20 μL pyridazine added to the 0.5 mol·L^{-1} H_2SO_4 electrolyte under 50 mA·cm^{-2} electrolysis conditions. ((b) and (c)) The fifth cyclic voltammetry curves for (b) RuO_2/CFP and (c) pyd-RuO_2/CFP at a scan rate of 50 mV·s^{-1} for 5 cycles. ((d) and (e)) Difference ATR-SEIRAS spectra of the RuO_2 in 0.5 mol·L^{-1} H_2SO_4 electrolyte (d) with and (e) without 20 μL pyridazine by sequential measurements. The spectra were subtracted by the spectrum taken at open circuit potential (OCP).

(Fig. 3(d)). The peaks at 3094 and 1582 cm^{-1} underwent gradual enhancement under more positive potentials, while the peak at 1440 cm^{-1} exhibited a concurrent gradual weakening. Comparing with the standard spectrum of pure pyridazine (Fig. S12 in the ESM), we confirmed the former originated from C–H stretching vibration and C–C ring stretching vibration of pyridazine, respectively, with the latter originated from the C–N ring stretching vibration of pyridazine. The enhanced signals were likely resulted from the enrichment of pyridazine with strong tendency toward chemisorption, while the diminished C–N stretching signal might be due to the coordination of pyridazine to RuO_2 surface that weakens the C–N bond.

After that, we switched the electrolyte from the pyridazine-containing electrolyte to a pure 0.5 mol·L^{-1} H_2SO_4 electrolyte. In contrast to the pyridazine etching situation, this scan showed the reverse trend with decreasing C–C stretching intensity at 1577 cm^{-1} and increasing C–N stretching intensity at 1432 cm^{-1}, corresponding to the pyridazine detachment in pure H_2SO_4 electrolyte (Fig. 3(e)). Comparatively, the C–H bonding peak at 3094 cm^{-1} almost disappeared during this can. We attributed this effect to the fact that the enrichment of C–H stretching is originated from the enriched pyridazine near the vicinity of electrode rather than the directly-adsorbed pyridazine, and once pyridazine is removed, this C–H stretching peak could totally disappear. These results confirm that the pyridazine could dynamically adsorb/desorb on the RuO_2 surface. In the pyridazine-containing electrolyte, the pyridazine tends to adsorb and stabilize on the RuO_2 surface, and only under highly anodic potentials, these pyridazine could desorb and drag the Ru to leach. While switching to the electrolyte not containing pyridazine, the anodic potential facilely drives its desorption for leaving the active site toward OER.

We have demonstrated the effectiveness of pyridazine adsorption for stabilizing the RuO_2 surface, but the facet selectivity upon OER stability and pyridazine etching remains to be addressed. Accordingly, we first gleaned the facet stability toward OER by TEM characterization (Figs. 4(a)–4(c)). The pyd-RuO_2 catalysts after 5 h stability measurement were characterized. High-angle annular dark-field (HAADF) imaging and EDS characterization revealed the slightly remnant N elemental distribution, but this distribution showed the absence of discernible regional specificity compared to Ru and O, suggesting the dynamic adsorption/desorption of pyridazine (Fig. S13 in the ESM). By magnifying the

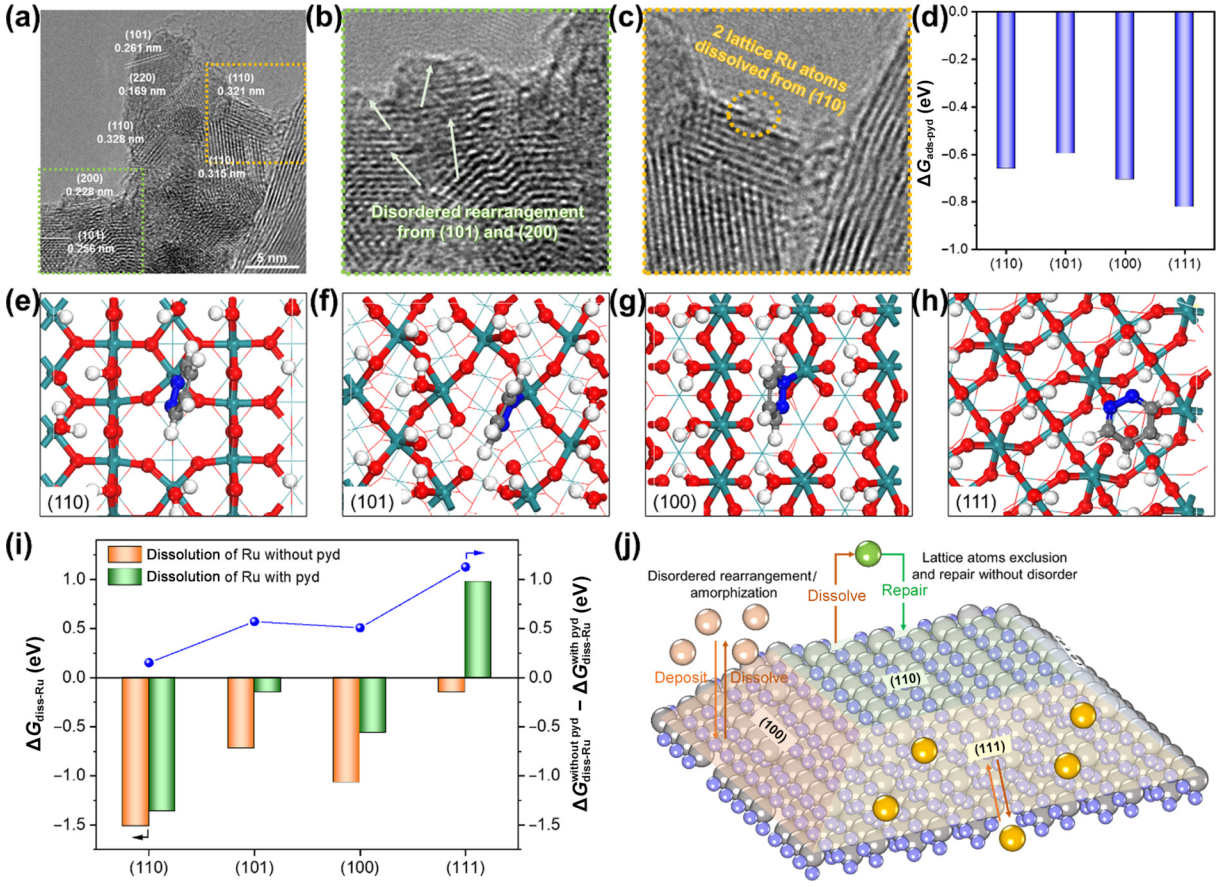

Figure 4 ((a)–(c)) TEM images of pyd-RuO_2/CFP electrode after 100 mA·cm^{-2} OER testing in 0.5 mol·L^{-1} H_2SO_4 electrolyte for 5 h. (d) Adsorption free energies of pyridazine ($\Delta G_{ads\text{-}pyd}$) on (110), (101), (100), and (111) surfaces by DFT calculations. ((e)–(h)) The configuration of Ru dissolved on (110), (101), (100), and (111) surfaces of RuO_2 in the presence of pyridazine. (i) The dissolution free energy of Ru ($\Delta G_{diss\text{-}Ru}$) in the absence (orange) and presence (green) of pyridazine on different RuO_2 facets. The blue dots represent the differences in dissolution energies of Ru in the absence and presence of pyridazine ($\Delta G^{withoutpyd}_{diss-Ru} - \Delta G^{withpyd}_{diss-Ru}$). (j) The schematic diagram of OER stability mechanisms on different RuO_2 facets.

edges of each facet on the RuO_2, we observed fuzzy crystalline surfaces on (101) and (200), corresponding to strongly disordered rearrangement and amorphization under OER conditions. These disordered lattices could lead to severe degradation of the OER activity and continuous dissolution of Ru (Fig. 4(b)). Comparatively, the edges of the (110) facet remained very clear, and two rows of Ru atoms were clearly plucked out of the plane toward dissolution. This phenomenon suggests that RuO_2 (110) is not perfectly stable but is subject to dissolution in a more ordered manner (Fig. 4(c)). Combining the stabilized Ru dissolution after hours of OER operation, we envision that the dissolved Ru can partially repair onto the RuO_2 (110) surface for reaching equilibrium. Whereas, on other facets, despite their possibly lower Ru dissolution, the surface Ru atoms can be subject to the significant rearrangement into amorphous structure toward instability.

To reveal the effect of pyridazine on the dissolution of Ru during etching, we carried out density functional theory calculation and constructed models of different RuO_2 facets with low Miller indices, including (110), (101), (100), and (111). The thermodynamically stable configurations of these surfaces were first determined in the absence of pyridazine molecules. The (100) and (111) surfaces exhibit stable configurations with 1 molecular layer (ML) H_2O^* coverage, whereas the (110) and (101) surfaces present 1/2 ML H_2O^* + 1/2(H^* + OH^*) configurations according to the global structure search using stochastic surface walking (SSW) based on neural network (NN) [46] (Figs. S14–S17 in the ESM). The dissolution energies ($\Delta G_{diss\text{-}Ru}$) of Ru atoms on these surfaces were then investigated based on the stable configurations. Ru atoms are most readily dissolved from the (110) surface, exhibiting the most exothermic $\Delta G_{diss\text{-}Ru}$ of −1.52 eV, while the $\Delta G_{diss\text{-}Ru}$ values for the (101), (100), and (111) surfaces are −0.72, −1.07, and −0.15 eV, respectively (Figs. 4(e)–4(h) and Figs. S18–S21 in the ESM).

In the presence of pyridazine molecule, pyridazine adsorption on each surface is exothermic and is accompanied by desorption of H_2O molecules from the adsorption sites (Fig. 4(d)). The dissolution of Ru in the presence of pyridazine was further explored (Figs. 4(e)–4(h) and Figs. S18–S21 in the ESM). The dissolution exotherms for Ru atoms on the (101), (100), and (111) surfaces under pyridazine are significantly reduced to −0.15, −0.56, and 0.98 eV, respectively (see the green bar in Fig. 4(i)), indicating a strong inhibition of Ru dissolution by pyridazine molecules. Notably, the exotherm of Ru dissolution on the (110) surface is only slightly reduced to −1.37 eV, implying less pronounced inhibition effect on the (110) surface. Consequently, the inhibition of Ru dissolution by pyridazine on the (101), (100), and (111) surfaces, but not on the (110) surface, contributes to the extensive exposure of (110) facet of RuO_2 under etching conditions.

By compiling the afore-mentioned results, we could depict a

vivid picture of facet-selective etching and OER activity facilitated by pyridazine (Fig. 4(j)). During the etching process, pyridazine dynamically adsorbs onto various facets of the RuO_2, more favorably onto the (100) and (111) facets. More importantly, the adsorption of pyridazine significantly stabilizes the Ru atoms on the surfaces, especially on the facets other than the (110) facet. As a result, the RuO_2 can be selectively etched along the direction perpendicular to the (110) plane to produce a (110) facet-enriched RuO_2 catalyst, pyd-RuO_2. Despite the high dissolution rate of Ru on the (110) facet, the (110)-enriched RuO_2 showed much enhanced stability toward OER over long terms. Upon OER operation, the adsorbed pyridazine could be facilely detached to expose more active sites. Ru atoms on the (110) surface can dynamically dissolve and repair in an ordered manner without much disruption of the surface structures, while Ru atoms on other surfaces tend to undergo disordered rearrangement, possibly via local dissolution and deposition into amorphized structures. These amorphized structures can continuously lose active Ru centers and corresponding OER stability. This explains our findings of more stable (110)-enriched RuO_2, as well as many literature reports.

3 Conclusions

Overall, we developed an effective strategy for enhancing the stability of RuO_2 by the facet-selective etching using pyridazine. The validity of this strategy was confirmed by the TEM characterization of enriched (110) facets and significantly longer OER operation with suppressed Ru dissolution. A combinatorial analytic technique of electrochemical measurement, *in situ* ATR-SEIRAS and XPS showed that pyridazine can facilely adsorb onto the RuO_2 surface to stabilize the surface atoms. This stabilization effect greatly differs on different facets, with a much less pronounced effect on the (110) facet, and therefore, the anodic etching process prefers to take the (110) direction for enriching the (110) facets for the pyd-RuO_2. This is corroborated by the calculated dissolution energies on different facets. Further analysis by TEM characterization and DFT calculation reveals that the (110) facet favorably undergoes the dissolution and repair cycle in an ordered manner, while other facets lead toward disorder and amorphization that devastates the OER stability. This discovery offers an insight into the dissolution and stability mechanism of RuO_2-based catalysts, as well as an effective strategy for enriching certain facets on polycrystalline nanoparticles by harnessing the power of surface ligands, especially toward facet-selective etching.

Electronic Supplementary Material: Supplementary material (additional electrochemical characterizations, TEM, HAADF, STEM images, and theoretical models) is available in the online version of this article at https://doi.org/10.26599/NR.2025.94907315.

Data availability

All data needed to support the conclusions in the paper are presented in the manuscript and the Electronic Supplementary Material. Additional data related to this paper may be requested from the corresponding author upon request.

Acknowledgements

This work was supported by the National Natural Science Foundation of China (No. 22172036) and the Fundamental Research Funds for the Central Universities (No. 20720220011).

Declaration of competing interest

All the contributing authors report no conflict of interests in this work.

Author contribution statement

X. T. C.: Experimental design and validation, data curation, visualization, formal analysis, visualization, manuscript writing. Y. K. K.: Experimental design and validation, visualization, formal analysis, manuscript writing. T. J.: Sample characterization for XPS, formal analysis, manuscript revising. Z. C.: Sample characterization for *in situ* IR, formal analysis, manuscript revising. Y. M. H.: Sample characterization for EIS, formal analysis, manuscript revising. S. S. C.: Sample characterization for *in situ* IR, formal analysis, manuscript revising. W. D.: Sample characterization for *in situ* IR, formal analysis, manuscript revising. Y. F. L.: Methodology, funding acquisition, supervision, manuscript revising. M. G.: Conceptualization, methodology, supervision, funding acquisition, manuscript revising. All of the authors discussed the results and commented on the paper. All the authors have approved the final manuscript.

Use of AI statement

None.

References

[1] Shih, A. J.; Monteiro, M. C. O.; Dattila, F.; Pavesi, D.; Philips, M.; Da Silva, A. H. M.; Vos, R. E.; Ojha, K.; Park, S.; Van Der Heijden, O. et al. Water electrolysis. *Nat. Rev. Methods Primers* **2022**, *2*, 84.

[2] Gan, T.; Wang, D. S. Atomically dispersed materials: Ideal catalysts in atomic era. *Nano Res.* **2024**, *17*, 18–38.

[3] Liu, Y. P.; Liang, X.; Chen, H.; Gao, R. Q.; Shi, L.; Yang, L.; Zou, X. X. Iridium-containing water-oxidation catalysts in acidic electrolyte. *Chin. J. Catal.* **2021**, *42*, 1054–1077.

[4] Tang, H. T.; Zhou, H. Y.; Pan, Y. M.; Zhang, J. L.; Cui, F. H.; Li, W. H.; Wang, D. S. Single-atom manganese-catalyzed oxygen evolution drives the electrochemical oxidation of silane to silanol. *Angew. Chem., Int. Ed.* **2024**, *63*, e202315032.

[5] Lin, H. Y.; Lou, Z. X.; Ding, Y. L.; Li, X. X.; Mao, F. X.; Yuan, H. Y.; Liu, P. F.; Yang, H. G. Oxygen evolution electrocatalysts for the proton exchange membrane electrolyzer: Challenges on stability. *Small Methods* **2022**, *6*, 2201130.

[6] Zeng, F.; Mebrahtu, C.; Liao, L. F.; Beine, A. K.; Palkovits, R. Stability and deactivation of OER electrocatalysts: A review. *J. Energy Chem.* **2022**, *69*, 301–329.

[7] Wang, Y.; Ma, F. Y.; Zhang, G. Q.; Zhang, J. W.; Zhao, H.; Dong, Y. M.; Wang, D. S. Precise synthesis of dual atom sites for electrocatalysis. *Nano Res.* **2024**, *17*, 9397–9427.

[8] Over, H. Surface chemistry of ruthenium dioxide in heterogeneous catalysis and electrocatalysis: From fundamental to applied research. *Chem. Rev.* **2012**, *112*, 3356–3426.

[9] Cherevko, S. Stability and dissolution of electrocatalysts: Building the bridge between model and "real world" systems. *Curr. Opin. Electrochem.* **2018**, *8*, 118–125.

[10] Wen, Y. Z.; Liu, C.; Huang, R.; Zhang, H.; Li, X. B.; García de Arquer, F. P.; Liu, Z.; Li, Y. Y.; Zhang, B. Introducing brønsted acid

sites to accelerate the bridging-oxygen-assisted deprotonation in acidic water oxidation. *Nat. Commun.* **2022**, *13*, 4871.

[11] Deng, L. M.; Hung, S. F.; Lin, Z. Y.; Zhang, Y.; Zhang, C. C.; Hao, Y. X.; Liu, S. Y.; Kuo, C. H.; Chen, H. Y.; Peng, J. et al. Valence oscillation of Ru active sites for efficient and robust acidic water oxidation. *Adv. Mater.* **2023**, *35*, 2305939.

[12] Wu, Z. Y.; Chen, F. Y.; Li, B. Y.; Yu, S. W.; Finfrock, Y. Z.; Meira, D. M.; Yan, Q. Q.; Zhu, P.; Chen, M. X.; Song, T. W. et al. Non-iridium-based electrocatalyst for durable acidic oxygen evolution reaction in proton exchange membrane water electrolysis. *Nat. Mater.* **2023**, *22*, 100–108.

[13] Liu, M. H.; Chen, X. X.; Li, S. Y.; Ni, C. D.; Chen, Y. W.; Su, H. Dynamic-cycling zinc sites promote ruthenium oxide for sub-ampere electrochemical water oxidation. *Nano Lett.* **2024**, *24*, 16055–16063.

[14] Burnett, D. L.; Petrucco, E.; Rigg, K. M.; Zalitis, C. M.; Lok, J. G.; Kashtiban, R. J.; Lees, M. R.; Sharman, J. D. B.; Walton, R. I. (M, Ru)O_2 (M = Mg, Zn, Cu, Ni, Co) Rutiles and their use as oxygen evolution electrocatalysts in membrane electrode assemblies under acidic conditions. *Chem. Mater.* **2020**, *32*, 6150–6160.

[15] Chen, S.; Huang, H.; Jiang, P.; Yang, K.; Diao, J. F.; Gong, S. P.; Liu, S.; Huang, M. X.; Wang, H.; Chen, Q. W. Mn-doped RuO_2 nanocrystals as highly active electrocatalysts for enhanced oxygen evolution in acidic media. *ACS Catal.* **2020**, *10*, 1152–1160.

[16] Sun, H. N.; Jung, W. Recent advances in doped ruthenium oxides as high-efficiency electrocatalysts for the oxygen evolution reaction. *J. Mater. Chem. A* **2021**, *9*, 15506–15521.

[17] Shi, Z. P.; Li, J.; Wang, Y. B.; Liu, S. W.; Zhu, J. B.; Yang, J. H.; Wang, X.; Ni, J.; Jiang, Z.; Zhang, L. J. et al. Customized reaction route for ruthenium oxide towards stabilized water oxidation in high-performance PEM electrolyzers. *Nat. Commun.* **2023**, *14*, 843.

[18] Du, K.; Zhang, L. F.; Shan, J. Q.; Guo, J. X.; Mao, J.; Yang, C. C.; Wang, C. H.; Hu, Z. P.; Ling, T. Interface engineering breaks both stability and activity limits of RuO_2 for sustainable water oxidation. *Nat. Commun.* **2022**, *13*, 5448.

[19] Ji, M. W.; Yang, X.; Chang, S. D.; Chen, W. X.; Wang, J.; He, D. S.; Hu, Y.; Deng, Q.; Sun, Y.; Li, B. et al. RuO_2 clusters derived from bulk $SrRuO_3$: Robust catalyst for oxygen evolution reaction in acid. *Nano Res.* **2022**, *15*, 1959–1965.

[20] Hubert, M. A.; Patel, A. M.; Gallo, A.; Liu, Y. Z.; Valle, E.; Ben-Naim, M.; Sanchez, J.; Sokaras, D.; Sinclair, R.; Nørskov, J. K. et al. Acidic oxygen evolution reaction activity–stability relationships in Ru-based pyrochlores. *ACS Catal.* **2020**, *10*, 12182–12196.

[21] Boakye, F. O.; Harrath, K.; Zhang, D. T.; You, Y.; Zhang, W. B.; Wang, Z.; Zhang, H. N.; Zhu, J. X.; Long, J. C.; Zhu, J. Q. et al. Synergistic engineering of dopant and support of Ru oxide catalyst enables ultrahigh performance for acidic oxygen evolution. *Adv. Funct. Mater.* **2024**, *34*, 2408714.

[22] Zhuang, J. H.; Wang, D. S. Recent advances of single-atom alloy catalyst: Properties, synthetic methods and electrocatalytic applications. *Mater. Today Catal.* **2023**, *2*, 100009.

[23] Lin, C.; Li, J. L.; Li, X. P.; Yang, S.; Luo, W.; Zhang, Y. J.; Kim, S. H.; Kim, D. H.; Shinde, S. S.; Li, Y. F. et al. *In-situ* reconstructed Ru atom array on α-MnO_2 with enhanced performance for acidic water oxidation. *Nat. Catal.* **2021**, *4*, 1012–1023.

[24] Yao, N.; Jia, H. N.; Zhu, J.; Shi, Z. P.; Cong, H. J.; Ge, J. J.; Luo, W. Atomically dispersed Ru oxide catalyst with lattice oxygen participation for efficient acidic water oxidation. *Chem* **2023**, *9*, 1882–1896.

[25] Liu, Y.; Huang, Y.; Wu, D. J.; Jang, H.; Wu, J. H.; Li, H. R.; Li, W. X.; Zhu, F.; Kim, M. G.; Zhou, D. L. et al. Ultrathin and conformal depletion layer of core/shell heterojunction enables efficient and stable acidic water oxidation. *J. Am. Chem. Soc.* **2024**, *146*, 26897–26908.

[26] Peng, C. L.; Zhao, W. P.; Li, Z. X.; Kuang, Z. Y.; Cheng, G. F.; Miller, J. T.; Sun, S. H.; Chen, H. R. Eutectic molten salt assisted synthesis of highly defective and flexible ruthenium oxide for efficient overall water splitting. *Chem. Eng. J.* **2021**, *425*, 131707.

[27] He, W. D.; Tan, X. H.; Guo, Y. Y.; Xiao, Y. H.; Cui, H.; Wang, C. X. Grain-boundary-rich RuO_2 porous nanosheet for efficient and stable acidic water oxidation. *Angew. Chem., Int. Ed.* **2024**, *63*, e202405798.

[28] Wu, M.; Fan, Y. Y.; Huang, Y.; Wang, D. X.; Xie, Y.; Wu, A. P.; Tian, C. G. Synergistic Ru/RuO_2 heterojunctions stabilized by carbon coating as efficient and stable bifunctional electrocatalysts for acidic overall water splitting. *Nano Res.* **2024**, *17*, 6931–6939.

[29] Shang, F. F.; He, H. J.; Lin, Y.; An, B.; Cai, H. R.; Li, X. Q.; Wang, W. T.; Liang, C.; Yang, S. C.; Wang, B. Hetero-nanojunction armored with carbon layer for boosting water oxidation over RuO_2 in acid. *Inorg. Chem. Front.* **2024**, *11*, 5265–5272.

[30] Klyukin, K.; Zagalskaya, A.; Alexandrov, V. Role of dissolution intermediates in promoting oxygen evolution reaction at RuO_2 (110) surface. *J. Phys. Chem. C* **2019**, *123*, 22151–22157.

[31] Roy, C.; Rao, R. R.; Stoerzinger, K. A.; Hwang, J.; Rossmeisl, J.; Chorkendorff, I.; Shao-Horn, Y.; Stephens, I. E. L. Trends in activity and dissolution on RuO_2 under oxygen evolution conditions: Particles versus well-defined extended surfaces. *ACS Energy Lett.* **2018**, *3*, 2045–2051.

[32] Stoerzinger, K. A.; Diaz-Morales, O.; Kolb, M.; Rao, R. R.; Frydendal, R.; Qiao, L.; Wang, X. R.; Halck, N. B.; Rossmeisl, J.; Hansen, H. A. et al. Orientation-dependent oxygen evolution on RuO_2 without lattice exchange. *ACS Energy Lett.* **2017**, *2*, 876–881.

[33] Xia, Y. N.; Xia, X. H.; Peng, H. C. Shape-controlled synthesis of colloidal metal nanocrystals: Thermodynamic versus kinetic products. *J. Am. Chem. Soc.* **2015**, *137*, 7947–7966.

[34] Gao, Y.; Yang, C. D.; Sun, F. L.; He, D. P.; Wang, X. Q.; Chen, J.; Zheng, X. B.; Liu, R. C.; Pan, H. G.; Wang, D. S. Ligand-tuning metallic sites in molecular complexes for efficient water oxidation. *Angew. Chem., Int. Ed.* **2025**, *64*, e202415755.

[35] Wang, L. G.; Wu, J. B.; Wang, S. W.; Liu, H.; Wang, Y.; Wang, D. S. The reformation of catalyst: From a trial-and-error synthesis to rational design. *Nano Res.* **2024**, *17*, 3261–3301.

[36] Qin, Y. L.; Yu, K. D.; Wang, G.; Zhuang, Z. C.; Dou, Y. H.; Wang, D. S.; Chen, Z. B. Adjacent-ligand tuning of atomically precise Cu–Pd sites enables efficient methanol electrooxidation with a CO-free pathway. *Angew. Chem., Int. Ed.* **2025**, *64*, e202420817.

[37] Quadri, T. W.; Akpan, E. D.; Elugoke, S. E.; Dagdag, O.; Nnaji, N. J.; Verma, C.; Olasunkanmi, L. O.; AlFantazi, A.; Anadebe, V. C.; Barik, R. C. et al. A critical review of coordination chemistry of pyrimidine and pyridazine compounds: Bonding, chelation and corrosion inhibition. *Coord. Chem. Rev.* **2025**, *523*, 216285.

[38] Chang, K. H.; Hu, C. C.; Chou, C. Y. Textural and capacitive characteristics of hydrothermally derived $RuO_2{\cdot}xH_2O$ nanocrystallites: Independent control of crystal size and water content. *Chem. Mater.* **2007**, *19*, 2112–2119.

[39] Mu, X. Q.; Zhang, X. Y.; Chen, Z. Y.; Gao, Y.; Yu, M.; Chen, D.; Pan, H. Z.; Liu, S. L.; Wang, D. S.; Mu, S. C. Constructing symmetry-mismatched $Ru_xFe_{3-x}O_4$ heterointerface-supported Ru clusters for efficient hydrogen evolution and oxidation reactions. *Nano Lett.* **2024**, *24*, 1015–1023.

[40] Zhang, Y.; Mu, X. Q.; Liu, Z. Y.; Zhao, H. Y.; Zhuang, Z. C.; Zhang, Y. F.; Mu, S. C.; Liu, S. L.; Wang, D. S.; Dai, Z. H. Twin-distortion modulated ultra-low coordination PtRuNi–O_x catalyst for enhanced hydrogen production from chemical wastewater. *Nat. Commun.* **2024**, *15*, 10149.

[41] Wang, K. X.; Wang, Y. L.; Yang, B.; Li, Z. J.; Qin, X. T.; Zhang, Q. H.; Lei, L. C.; Qiu, M.; Wu, G.; Hou, Y. Highly active ruthenium sites

stabilized by modulating electron-feeding for sustainable acidic oxygen-evolution electrocatalysis. *Energy Environ. Sci.* **2022**, *15*, 2356–2365.

[42] Jin, H.; Choi, S.; Bang, G. J.; Kwon, T.; Kim, H. S.; Lee, S. J.; Hong, Y.; Lee, D. W.; Park, H. S.; Baik, H. et al. Safeguarding the RuO_2 phase against lattice oxygen oxidation during acidic water electrooxidation. *Energy Environ. Sci.* **2022**, *15*, 1119–1130.

[43] Rochefort, D.; Dabo, P.; Guay, D.; Sherwood, P. M. A. XPS investigations of thermally prepared RuO_2 electrodes in reductive conditions. *Electrochim. Acta* **2003**, *48*, 4245–4252.

[44] He, J. Y.; Chen, W. X.; Gao, H. M.; Chen, Y. X.; Zhou, L.; Zou, Y. Q.; Chen, R.; Tao, L.; Lu, X.; Wang, S. Y. Tuning hydrogen binding modes within RuO_2 lattice by proton and electron Co-doping for active and stable acidic oxygen evolution. *Chem. Catal.* **2022**, *2*, 578–594.

[45] Stoerzinger, K. A.; Rao, R. R.; Wang, X. R.; Hong, W. T.; Rouleau, C. M.; Shao-Horn, Y. The role of Ru redox in pH-dependent oxygen evolution on rutile ruthenium dioxide surfaces. *Chem* **2017**, *2*, 668–675.

[46] Huang, S. D.; Shang, C.; Kang, P. L.; Zhang, X. J.; Liu, Z. P. LASP: Fast global potential energy surface exploration. *WIREs Comput. Mol. Sci.* **2019**, *9*, e1415.